Luo et al. *Zool. Res.* 2025, 46(5): 1079−1092
https://doi.org/10.24272/j.issn.2095-8137.2025.019
https://cstr.cn/32248.14.zr.2025.019

ZR | Zoological Research

Article Open Access

Testis-specific protein HSF5 is essential for proper chromatin organization and transcriptional reprogramming to drive pachynema progression

Chun-Hai Luo[1,#], Zhi-Wei Fan[1,#], Zi-Qi Yu[1,#], Da-Lin Liu[1], Hao-Ran Xu[1], Shu-Min Zhou[1], Xuan-Jing Zhu[1], Han-Chao Liu[1], Li-Fu Shao[1], Zhe-An Li[1], Chong Xie[1,*], Jun-Feng Zhan[1,*], Fei Sun[1,*]

[1] *Department of Urology & Andrology*, *Sir Run Run Shaw Hospital*, *Zhejiang University School of Medicine*, *Hangzhou*, *Zhejiang* 310016, *China*

ABSTRACT

Chromatin remodeling and transcriptional reprogramming play critical roles during mammalian meiotic prophase I; however, the precise mechanisms regulating these processes remain poorly understood. Our previous work demonstrated that deletion of heat shock factor 5 (HSF5), a member of the heat shock factor family, induces meiotic arrest and male infertility. However, the molecular pathways through which HSF5 governs meiotic progression have not yet been fully elucidated. In this study, a comprehensive multi-omics approach was applied to investigate the role of HSF5 in modulating chromatin dynamics and transcriptional reprogramming during pachynema progression. Analysis of ATAC-seq and single-cell RNA sequencing data revealed significant alterations in chromatin accessibility and disruption of the transcriptional regulatory network (TRN) in *Hsf5*$^{-/-}$ spermatocytes. Additionally, HSF5 deficiency resulted in defective XY body formation and altered histone modifications. Notably, *Hsf5*$^{-/-}$ spermatocytes also exhibited abnormal spermatoproteasome activity specifically on sex chromosomes, with evidence indicating that HSF5 may form a complex with USP7 *in vivo* to suppress H2AK119ub on meiotic sex chromosomes. These findings provide new insights into the complex, multifunctional role of HSF5 in regulating key meiotic events and advancing our understanding of its function during pachynema progression.

Keywords: HSF5; Cell biology; Molecular biology; Meiosis; XY body formation; Transcriptional regulatory network

INTRODUCTION

Meiosis is a highly specialized cell division process that reduces diploid cells to haploid gametes, ensuring the transfer of genetic material across generations and promoting genetic diversity through recombination. This intricate process begins with a single round of DNA replication, followed by two distinct division events—meiosis I and II—culminating in the formation of haploid cells (Zickler and Kleckner, 2015). Following the pre-meiotic S phase, primary germ cells enter an extended prophase I, during which chromatin organization undergoes dynamic reorganization. At leptotene, homologous recombination is initiated by the introduction of programmed DNA double-strand breaks (DSBs), facilitating DNA segment pairing. As homologous chromosomes align during the zygotene stage of meiosis, the axial element elongates along the chromosome axis, facilitating the formation of the synaptonemal complex, which mediates homolog pairing and recombination. Once synapsis is complete, cells transition to pachytene, during which crossover recombination occurs, followed by synaptonemal complex asymmetrical disassembly in the subsequent diplotene phase. Synaptonemal complex proteins persist at designated chromosomal subdomains until diakinesis, at which point chromosomes undergo further compaction and bivalents detach from the nuclear envelope to initiate homolog segregation (Dia et al., 2017). Pachytene, the longest of the five stages, lasting approximately 6 days in mice (Goetz et al., 1984), is characterized by the completion of homologous synapsis, crossover recombination, and “XY body” formation (Handel, 2004; Xie et al., 2022). Correspondingly, throughout pachytene, several surveillance mechanisms operate to ensure proper chromatin dynamics

Received: 28 February 2025; Accepted: 12 March 2025; Online: 13 March 2025

Foundation items: This work was supported by the National Natural Science Foundation of China (U24A20657, 82371613 to F.S.; 82301798), Key Research and Development Program of Zhejiang Province (2023C03035 to F.S.), China Post-doctoral Science Foundation (2022M722767), and Fellowship of China National Postdoctoral Program for Innovative Talents (BX20230314)

[#]Authors contributed equally to this work

*Corresponding authors, E-mail: ucla_2008@hotmail.com; jf_zhan3322103srrsh@zju.edu.cn; sunfeisrrsh@zju.edu.cn

and meiotic progression. These include critical checkpoints such as the DNA damage checkpoint, synapsis checkpoint, and meiotic sex chromosome inactivation (MSCI), all of which play essential roles in coordinating these processes (Roeder and Bailis, 2000; Turner, 2015; Xie et al., 2022).

During pachynema progression, chromatin undergoes dynamic reorganization, accompanied by distinct epigenetic modifications and transcriptional changes that collectively regulate meiotic progression (Rathke et al., 2014; Tahmasbpour Marzouni et al., 2022; Wang et al., 2024). The X and Y chromosomes are sequestered into a membraneless domain within the nucleus, forming the XY body, a structure central to MSCI. MSCI is initiated when ATR phosphorylates H2AX, which then recruits MDC1 to γH2AX, leading to the silencing of sex chromosomes (Blanco-Rodríguez, 2009; Handel, 2020; Ichijima et al., 2011; Turner, 2015). A recent study proposed that MSCI precedes the formation of the XY body, refining our understanding of the sequence of these events (Abe et al., 2020). Furthermore, XY body formation is closely associated with various histone modifications, including ubiquitination and methylation, with liquid-liquid phase separation (LLPS) recently proposed as a potential mechanism underlying both its formation and function (Alavattam et al., 2022; Page et al., 2012; Rao et al., 2017; Wu et al., 2020). These findings suggest that chromatin organization during pachynema is more complex and multifactorial than previously understood, involving a combination of biochemical modifications and structural dynamics. Various studies have reported significant changes in gene expression during prophase I, with transcriptional activity remaining low in the early stages (leptonema, zygonema, and early pachynema) before resuming at the mid-pachytene (Green et al., 2018; Hong et al., 2022; Shima et al., 2004). During pachynema progression, a distinct shift occurs in gene expression, characterized by a substantial down-regulation of genes involved in meiosis, with a concurrent up-regulation of genes essential for spermiogenesis (Da Cruz et al., 2016; Guo et al., 2022). This shift highlights the dynamic and tightly regulated nature of transcriptional reprogramming during this critical phase of germ cell development. The transcriptional regulatory network (TRN) orchestrates this complex gene expression pattern, playing a central role in the regulation of meiotic progression and ensuring proper progression through pachynema (Carrell, 2008; Hamazaki et al., 2021; Wang et al., 2024). Despite significant advances, the specific molecular mechanisms governing chromatin reorganization and transcriptional regulation in pachynema remain largely unexplored and require further investigation.

Our previous work revealed that heat shock factor 5 (HSF5), a member of the heat shock factor family, acts as a critical transcription regulator of genes essential for the progression of pachynema progression. By binding to specific promoter regions, HSF5 governs a diverse array of transcriptional programs that orchestrate both gene repression and activation (Luo et al., 2024). Notably, HSF5 exerts a repressive effect on genes such as *Sycp1*, *Meiob*, *Msh4*, and *Hat1*, leading to a decline in their transcriptional activity at key meiotic stages. In contrast, during the mid-to-late pachytene phase, HSF5 facilitates the expression of genes, including *Hspa2*, *Ccnb1* and *Plk1*, to prepare for subsequent transition to desynapsis (Luo et al., 2024). When HSF5 is absent, a profound meiotic arrest at the mid-to-late pachytene stage, resulting in the significant depletion of pachytene spermatocytes during prophase I. This occurs despite normal homologous chromosome pairing, synapsis, and MSCI-associated immunofluorescence (IF) signals, indicating that the role of HSF5 extends beyond these processes (Luo et al., 2024). In this study, we demonstrated that HSF5 likely mediates pachynema progression via its regulation of chromatin dynamics and transcriptional reprogramming. Notably, in *Hsf5*$^{-/-}$ spermatocytes, global chromatin accessibility and the TRN were disrupted, with XY chromosome-associated behaviors, such as XY body formation, spermatoproteasome activity, and epigenetic modifications (including H2AK119ub and K48ub), showing abnormal alteration.

MATERIALS AND METHODS

Mice and ethics statement

All procedures involving mice were approved by the Tab of Animal Experimental Ethical Inspection at Sir Run Run Shaw Hospital, Zhejiang University School of Medicine (approval no: NO:SRRSH2025-0006), and were conducted in accordance with the Guide for the Care and Use of Laboratory Animals. Mice were maintained in a specific pathogen-free facility at Zhejiang University School of Medicine. The *Hsf5*$^{-/-}$ mouse model was generated by Shanghai Model Organisms Center, Inc. (China). Briefly, Cas9 mRNA was transcribed *in vitro* using an mMESSAGE mMACHINE T7 Ultra Kit (Ambion, USA) according to the manufacturer's instructions. Two sgRNAs were transcribed *in vitro* using a MEGAshortscript Kit (Thermo Fisher, USA): one targeting intron 2 of *Hsf5* (5'-GCTGTATCTTACTTGGTTGA CGG-3') and one targeting intron 3 of *Hsf5* (5'-AGTAGAAGCCAAAGATAGCT GGG-3'). Cas9 mRNA and sgRNAs were microinjected into zygotes from C57BL/6J mice and transferred to pseudo-pregnant recipients. F0 offspring were screened by polymerase chain reaction (PCR) and sequencing using the primer pair: F-5'-AGCTCAAGAGGGAGGGAGAG-3'; R-5'-AGGCAGAGACATA GGGAGCA-3'. Positive F0 mice were crossed with C57BL/6J mice to obtain F1 heterozygous *Hsf5* knockout mice. F1 genotypes were determined by PCR and confirmed by sequencing. Male and female F1 heterozygous mice were intercrossed to produce homozygous *Hsf5*$^{-/-}$ mice.

Isolation of pachytene spermatocytes

Pachytene spermatocytes were isolated by bovine serum albumin (BSA) gradient sedimentation (STA-PUT), as described in previous research (Luo et al., 2024). Testes (n=8) from four adult male mice (postnatal day 56, P56) were excised after euthanasia, decapsulated, rinsed in ice-cold phosphate-buffered saline (PBS) supplemented with 1× penicillin-streptomycin (Biochannel, BC-CE-007, China), and digested in Krebs-Ringer solution containing collagenase (0.5 mg/mL) at 33°C for 15 min to isolate seminiferous tubules. Tubules were further digested with trypsin (0.5 mg/mL) and DNase I (1 mg/mL) for 10 min, passed through a 40 μm nylon cell strainer, and resuspended in Krebs-Ringer solution containing 0.5% BSA. The single-cell suspension was separated by unit-gravity sedimentation for 3 h using the STA-PUT apparatus with a 2%–4% BSA gradient. Viability was assessed by trypan blue exclusion (Sunncell, SNK-004, China). Pachytene spermatocytes were identified based on characteristic morphology (12–18 μm in diameter) and by IF staining patterns with DAPI and γH2AX. Fractions enriched for pachytene cells were pooled for downstream analyses.

Assay for transposase-accessible chromatin with high-throughput sequencing (ATAC-seq) library preparation and sequencing

ATAC-seq was performed with the Hyperactive ATAC-Seq Library Prep Kit for Illumina (Vazyme, TD711, China) following the manufacturer's instructions and published workflow (Corces et al., 2017). Approximately 5×10^5 STA-PUT-isolated pachytene spermatocytes were washed in 500 μL of PBS, centrifuged at 500 ×*g* for 30 min at 4°C, resuspended in 50 μL of cold lysis buffer, and incubated on ice for 10 min to isolate the nuclei. After centrifugation, the nuclei were subjected to transposition in 50 μL of Tn5 transposase reaction mix at 37°C for 30 min. The reaction was terminated with stop buffer at room temperature for 5 min. Adapter-ligated DNA fragments were extracted and PCR-amplified with indexing primers (Vazyme, TD202, China). The amplified DNA was size-selected (200–800 bp) using VAHTS DNA Clean Beads (Vazyme, N411-01, China), and DNA quantity was assessed using a Qubit™4 Fluorometer (Invitrogen, USA) and Bioanalyzer 2100 (Agilent, USA). Libraries were sequenced on the Illumina platform (USA) by Genedenovo Biotechnology (China).

ATAC-seq data analyses

Raw reads were processed with Fastp (v.0.23.4) for quality control (Chen, 2023), including adapter removal and trimming of low-quality bases. Quality-filtered reads were aligned to the mouse reference genome (mm39, Gencode, vM33) using STAR (v.2.7.11b) with the parameters: "--alignEndsType Local --outFilterMismatchNmax 10 --outFilterMultimapNmax 1 --alignMatesGapMax 700 --alignSJoverhangMin 10". SAMtools (v.1.19.2) was used to calculate read coverage and depth (Dobin et al., 2013; Li et al., 2009). PCR duplicate reads and reads overlapping blacklist regions were filtered using Bedtools (Amemiya et al., 2019). The filtered reads were converted to BED format, and peaks were called using MACS2 with the parameters: "--nomodel --shift -100 --extsize 200 -B --SPMR". Differential ATAC-seq regions were identified using DiffBind (v.3.16.0) (Ross-Innes et al., 2012) using absolute log2 fold change greater than 1 and false discovery rate (FDR) less than 0.01 as thresholds. Subsequently, peak regions were annotated against the reference annotation dataset Gencode_vM33 with ChIPseeker (v.1.42.0) (Wang et al., 2022). Known motif discovery within peak regions was assessed using findMotifsGenome.pl in Homer (v.4.11) with default parameters (Heinz et al., 2010). Additionally, the DeepTools (v.3.5.4) bamCoverage function was used to generate ATAC-seq signal track files in BigWig format (Ramírez et al., 2016). Heatmaps of signals across all transcription start sites (TSSs) and peak summits were generated using the computeMatrix and plotHeatmap functions in DeepTools.

Spermatocyte spreading and IF staining

For frozen section IF, testes (P56 and P21) were fixed in Bouin's solution, dehydrated with increasing sucrose concentrations, and embedded in Tissue-Tek OCT compound. Cryosections (5 μm) were mounted onto slides, subjected to antigen retrieval, and washed three times with PBS. The sections were then incubated with primary antibodies overnight at 4°C in a humidified chamber, washed, and incubated with secondary antibodies for 2 h at room temperature. For spermatocyte spreading (Dia et al., 2017), testes were dissected, with seminiferous tubules washed in PBS and incubated in a hypotonic extraction buffer on ice for 45 min. The tubules were minced in 100 mM sucrose and pipetted to release germ cells, which were spread onto slides containing 1% paraformaldehyde (PFA) and 0.15% Triton X-100, followed by overnight incubation at 4°C. After incubation, the slides were washed with Photo-Flo 200, air-dried, and stored at −80°C.

The antibodies used for IF included: mouse anti-HSF5 (1:100, homemade), rat anti-H1t (1:100, homemade), rabbit anti-BRCA1 (1:100, homemade), rabbit anti-SYCP3 (1:200, Abcam, ab15093, UK), mouse anti-SYCP3 (1:200, Abcam, ab97672, UK), rabbit anti-γH2AX (1:200, Abcam, ab11174, UK), rabbit anti-MDC1 (1:200, Proteintech, 24721-1-AP, China), rabbit anti-SUMO1 (1:200, ABclonal, A19121, China), rabbit anti-SUMO2/3 (1:200, ABclonal, A22734, China), mouse anti-FK2 (1:200, Millipore, 4263, USA), mouse anti-E65C (1:200, Millipore, 05-678, USA), rabbit anti-H2AK119ub (1:200, Cell Signaling Technology, 8240, USA), rabbit anti-K48ub (1:200, Abmart, TC63005S, China), rabbit anti-PSMB2 (1:200, ABclonal, A13630, China), rabbit anti-PSMA7 (1:200, ABclonal, A4052, China), rabbit anti-RNF2 (1:200, ABclonal, A5563, China), rabbit anti-USP7 (1:200, ABclonal, A3448, China), rabbit anti-macroH2A.1 (1:200, ABclonal, A7045, China), rabbit anti-ATR (1:200, ABclonal, A22124, China), rabbit anti-H3K9me1 (1:100, ABclonal, A2358, China), rabbit anti-H3K9me2 (1:100, Affinity, DF6937, China), rabbit anti-H3K27ac (1:200, ABclonal, A7253, China), donkey anti-rabbit Alexa Fluor™ 488 (1:500, Thermo Fisher, A-21206, USA), donkey anti-mouse Alexa Fluor™ 555 (1:500, Thermo Fisher, A-31570, USA), and donkey anti-rat Alexa Fluor™ 647 (1:500, Thermo Fisher, A-48272, USA). Photomicrographs were captured using a confocal fluorescence microscope (Zeiss, LSM980, Germany).

Proteasome assay

Assays were performed in 96-well plates with a total volume of 150 μL. Reaction mixtures contained 26S buffer (2 mmol/L ATP, 25 mmol/L HEPES, 0.5 mmol/L EDTA, and 0.01% SDS, pH 7.5) and 50 μg of protein supernatant extracted from STA-PUT-isolated spermatocytes in lysis buffer (20 mmol/L Tris-HCl (pH 7.4), 150 mmol/L NaCl, 1% Nonidet P-40, and 1 mmol/L EDTA), followed by incubation at 37°C for 20 min. Fluorescently labeled substrates were added at 100 μmol/L final concentration to measure proteasome activities: Suc-Leu-Leu-Val-Tyr-7-amino-4-methylcoumarin (LLVY) for chymotrypsin-like (β5), Z-Ala-Arg-Arg-AMC (ARR) for trypsin-like (β2), and Z-Leu-Leu-Glu-AMC (LLE) for caspase-like (β1) activities (MCE; HY-P1002, HY-134961, HY-123053; USA). Free 7-amino-4-methylcoumarin (AMC) release was measured in 96-well plates (SAINING Biotechnology, AB2040320, China) using a Synergy H1 Multi-Mode Microplate Reader (Bio-Tek, USA) with 350 nm excitation and 440 nm emission, according to the manufacturer's protocols. Data were normalized against the background signal, which was corrected by subtracting values obtained without protein.

Extraction and analysis of histones

Purified pachytene spermatocytes (2×10^7) were washed twice with ice-cold PBS, resuspended in buffer A (250 mmol/L sucrose, 50 mmol/L KCl, 15 mmol/L NaCl, 10 mmol/L Tris-HCl (pH 7.4), 5 mmol/L $MgCl_2$, 1 mmol/L $CaCl_2$, 0.5% Triton X-100, 1 mmol/L DTT, 0.1 mmol/L PMSF, and 1× protease inhibitor), and incubated on ice for 10 min to release nuclei. After centrifugation at 1 000 ×*g* for 10 min at 4°C, the pellet

was washed with 1 000 μL of buffer A, followed by 1 000 μL of buffer B (10 mmol/L Tris-HCl (pH 7.4), 100 mmol/L NaCl, 5 mmol/L $MgCl_2$, 10 mmol/L $CaCl_2$, 300 mmol/L sucrose, 0.1 mmol/L PMSF, and 1×protease inhibitor) to remove Triton X-100. The nuclei were resuspended in 200 μL of buffer B, treated with 5 μL of MNase (200 U/μL), and incubated at 37°C with shaking (800 r/min) for 20 min. Following centrifugation at 1 000 ×*g* for 10 min at 4°C, the pellet was resuspended in 100 μL of histone extraction buffer (20 mmol/L Tris-HCl (pH 7.9), 10 mmol/L EDTA, and 0.5 mol/L KCl), incubated on ice for 20 min, and centrifuged at 16 000 ×*g* for 5 min at 4°C. After protein quantification, 5 μg of histones were subjected to 15% sodium dodecyl sulfate-polyacrylamide gel electrophoresis (SDS-PAGE) and Coomassie Brilliant Blue staining.

Transmission electron microscopy (TEM)

TEM was performed as described previously (Zhang et al., 2020), with minor modifications. Briefly, mouse testes (P70) were cut into small pieces (approximately 2 mm long×2 mm wide×2 mm high) and fixed in 0.1 mol/L phosphate buffer (PB, pH 7.4) containing 4% PFA, 4% glutaraldehyde, and 0.2% picric acid at 4°C for at least 12 h. After three washes with 0.1 mol/L PB, samples were post-fixed with 1% OsO4, dehydrated, and infiltrated with a mixture of acetone and Epon resin. The samples were embedded and sectioned into ultrathin slices (70 nm), followed by staining with uranyl acetate and lead citrate. Ultrastructure was analyzed using a TEM at 100 kV (Tecnai spirit, USA).

***In vivo* ubiquitylation assay**

The coding sequence of *Hsf5* was cloned into pFLAG-CMV-4 (Tsingke Biotech, China). HEK293T cells (Pricella Life Science & Technology, CL-0005, China) were co-transfected in 6-well plates (Jet Biofil, CAP011006, China) with 2 μg of pCMV6-HSF5-Flag and 2 μg of each of the following constructs: pCMV-HA-ubiquitin (WT), pCMV-HA-ubiquitin (K48), and pCMV-HA-ubiquitin (K48R). After 36 h, the cells were harvested and lysed in 500 μL of lysis buffer (20 mM Tris-Cl (pH 7.4), 150 mmol/L NaCl, 1% NP-40, 0.25% SDC, 5% glycerol, 1 mmol/L DTT, and 1× protease inhibitor) on ice for 10 min. Ectopic HSF5 was immunoprecipitated from these lysates at 4°C overnight, following the immunoprecipitation method described above. The beads were washed with washing buffer, boiled in SDS sample buffer, and the eluted proteins were analyzed by western blotting.

Co-immunoprecipitation (Co-IP) and western blotting (WB)

Co-IP was performed using the Absin Co-IP Kit (Absin, abs9649, China) with minor modifications. STA-PUT-isolated spermatocytes (1×10^7) were homogenized in 1 000 μL of lysis buffer (20 mmol/L Tris-Cl (pH 7.4), 150 mmol/L NaCl, 1% NP-40, 0.25% SDC, 5% glycerol, 1 mmol/L DTT, and 1 ×protease inhibitor), incubated on ice for 30 min, and centrifuged at 10 000 ×*g* for 10 min at 4°C. The supernatant was precleared with protein A/G beads, incubated overnight at 4°C with primary antibodies, and then with protein A/G beads for 4 h at 4°C. Beads were washed three times with high-salt Co-IP wash buffer (20 mmol/L Tris-Cl (pH 7.4), 300 mmol/L NaCl, 1% NP-40, 0.25% SDC, 5% glycerol, 1 mmol/L DTT, and 1× protease inhibitor). Bound proteins were subsequently eluted from the beads using 2× SDS gel-loading buffer. For plasmid-transfected cells (6-cm dishes), lysates were prepared in 500 μL lysis buffer and processed as above. Inputs and eluates were separated by SDS-PAGE, transferred to polyvinylidene fluoride (PVDF) membranes, blocked in PBST with 5% nonfat milk, incubated overnight at 4°C with primary antibodies, washed three times with PBST, then incubated with horseradish peroxidase (HRP)-conjugated secondary antibodies. Protein detection was performed using an Omni-ECL™ Femto Light Chemiluminescence Kit (Epizyme, SQ201, China) and imaged with the Bio-Rad ChemiDoc system. Antibodies used for Co-IP and WB included: rabbit anti-HSF5 (1:1 000 for WB, 1:200 for Co-IP, homemade), rabbit anti-γH2AX (1:1 000, Abcam, ab11174, UK), rabbit anti-H1t (1:1 000, ABclonal, A18597, China), rabbit anti-macroH2A.1 (1:1 000, ABclonal, A7045, China), rabbit anti-USP7 (1:1 000 for WB, 1:200 for Co-IP, ABclonal, A3448, China), rabbit anti-GAPDH (1:2 000, FineTest, FNab03342, China), rabbit HA-tag (1:2 000, Bioworld, AP0005, USA), mouse FLAG-tag (1:2 000, Sino Biological, 109143-MM13, China), HRP-conjugated Affinipure goat anti-mouse IgG(H+L) (1:5 000, Proteintech, SA00001-1, China), and HRP-conjugated Affinipure goat anti-rabbit IgG (H+L) (1:5 000, Proteintech, SA00001-2, China).

Statistical analysis

All experiments were performed independently at least three times. Data in figures are presented as mean±standard deviation (SD), unless stated otherwise. Statistical analyses were conducted using GraphPad Prism v.10, with comparisons between experimental groups conducted as specified in the figure legends.

RESULTS

Landscape of chromatin accessibility in *Hsf5*$^{+/+}$ and *Hsf5*$^{-/-}$ pachytene spermatocytes

Our previous study demonstrated that deletion of *Hsf5* disrupts the transcriptomic profiles of pachynema and alters the transcriptional dynamics of genes that drive pachynema progression (Luo et al., 2024). To investigate whether this dysregulation results from alterations in chromatin accessibility, ATAC-seq was used to compare the genomic chromatin accessibility landscapes between *Hsf5*$^{+/+}$ and *Hsf5*$^{-/-}$ pachytene spermatocytes. High-purity pachytene spermatocytes (approximately 78%) were first isolated from P56 testes by STA-PUT (Supplementary Figure S1A–C) and used for ATAC-seq. Two independent biological replicates demonstrated strong concordance, confirming their suitability for data integration (Supplementary Figure S1D).

MACS2 detected 37 025 peaks in *Hsf5*$^{+/+}$ and 64 111 peaks in *Hsf5*$^{-/-}$ (Figure 1A). In *Hsf5*$^{+/+}$, peak annotations were predominantly enriched at promoters (−3 000 bp to +3 000 bp of TSSs, 57.5%), untranslated regions (UTRs) (1.06%), exons (3.07%), introns (13.34%), and intergenic regions (25.04%) (Supplementary Figure S1E). In *Hsf5*$^{-/-}$, peaks were enriched in promoters (49.71%), UTRs (1.8%), exons (4.74%), introns (16.68%), and intergenic regions (27.08%) (Supplementary Figure S1F). Most peaks exhibited significant overlap with gene TSSs across chromosomes (Supplementary Figure S1G), consistent with enrichment of ATAC signal at TSSs during spermatogenesis (Maezawa et al., 2018). Despite broadly similar genomic distributions (Supplementary Figure S1E–G), global accessibility increased in *Hsf5*$^{-/-}$ compared with *Hsf5*$^{+/+}$ (35 050 regions gained accessibility and 925 regions lost accessibility; FDR<0.05 and fold change≥1) (Figure 1A; Supplementary Figure S1H), with a particularly

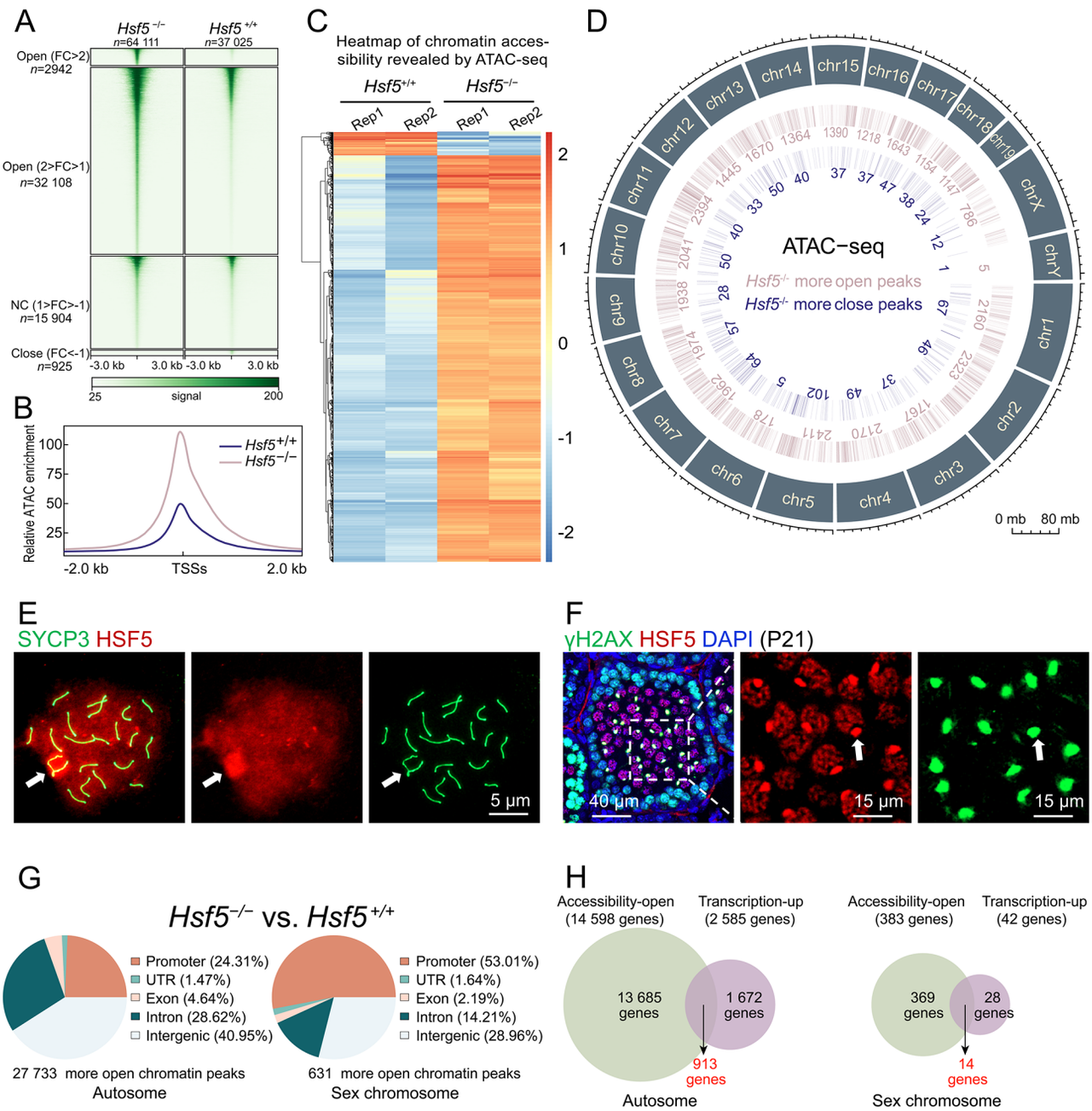

Figure 1 Chromatin accessibility and multi-omics analysis of *Hsf5*$^{+/+}$ and *Hsf5*$^{-/-}$ pachytene spermatocytes

A: Heatmap showing ATAC peaks based on changes in *Hsf5*$^{-/-}$ and *Hsf5*$^{+/+}$ pachytene cells. Each row represents a locus; green gradient indicates ATAC-seq signal intensity. B: Metaplot showing ATAC-seq signals at TSSs in *Hsf5*$^{+/+}$ and *Hsf5*$^{-/-}$ cells. C: Heatmap of two independent ATAC-seq analyses based on normalized $\log_2$(RPM) values of *Hsf5*$^{+/+}$ and *Hsf5*$^{-/-}$ cells. Total number of differentially accessible ATAC peaks in *Hsf5*$^{-/-}$ cells was 35 975, with 35 050 being more open and 925 being more closed. D: Distribution of 35 975 differentially accessible peaks across chromosomes. E: HSF5 staining with SYCP3 on chromosome spreads of pachytene spermatocytes from adult *Hsf5*$^{+/+}$ testes. Arrow indicates XY body. Scale bars are shown. F: γH2AX staining with HSF5 on testis sections at P21. Right two panels show magnifications of boxed areas in the left panel. Arrow indicates XY body. Scale bars are shown. G: Distributions of more open ATAC-seq peaks on autosomes and sex chromosomes in *Hsf5*$^{-/-}$ vs. *Hsf5*$^{+/+}$ pachytene cells. Two sets of data were normalized and combined for analysis. H: Venn diagrams of up-regulated genes from scRNA-seq (pachytene) data and genes with more open ATAC peaks.

pronounced increase at TSSs (Figure 1B). Heatmaps of normalized signal (reads per million mapped reads, RPM) centered on peaks corroborated widespread accessibility gains (Figure 1C). Differentially accessible peaks (35 975 total) were evenly distributed across chromosomes without detectable chromosomal bias (Figure 1D). Taken together, these results indicate that *Hsf5* deletion alters overall chromatin accessibility in spermatocytes, leading to a generally more open chromatin structure, particularly at TSSs, although a minority of loci exhibited reduced accessibility.

Multi-omics data integration reveals distinct regulation of chromatin accessibility and transcription on autosomes and sex chromosomes by HSF5

Given the distinct chromatin accessibility characteristics of autosomes and sex chromosomes in spermatocytes (Maezawa et al., 2018) and the marked enrichment of HSF5

on the XY chromosomes (Figure 1E, F), newly accessible peaks in *Hsf5*$^{-/-}$ were stratified by chromosome class and analyzed separately for autosomes and XY chromosomes. As shown in Figure 1G, compared with *Hsf5*$^{+/+}$ pachytene cells, autosomes in *Hsf5*$^{-/-}$ pachytene cells exhibited 27 733 open chromatin peaks, whereas the XY chromosomes contained 631 open chromatin peaks. Notably, open peaks on the sex chromosomes were substantially more enriched in promoter regions, accounting for 53.01% compared with only 24.31% enrichment on autosomes (Figure 1G). These data indicate a genome-wide increase in chromatin accessibility across autosomes and the XY chromosomes, with promoter regions on the sex chromosomes showing a disproportionate gain in *Hsf5*$^{-/-}$ pachytene cells relative to *Hsf5*$^{+/+}$.

To determine whether accessibility changes were associated with the transcriptional expression of corresponding genes, previously generated 10x Genomics single-cell RNA-seq (scRNA-seq) data (Luo et al., 2024) were integrated with ATAC-seq. In *Hsf5*$^{+/+}$, early (eP), middle (mP), and late pachytene (lP) clusters were merged into a single pachytene group, while in *Hsf5*$^{-/-}$, the eP and pachytene-like clusters were merged. Differentially expressed genes (DEGs) were defined using adjusted P<0.01 and |fold change|>1, yielding 2 627 up-regulated genes (2 585 autosomal and 42 XY-linked) and 3 013 down-regulated genes (2 944 autosomal and 64 XY-linked) (Supplementary Table S1). Expression shifts for autosomal and XY-linked genes were broadly similar between genotypes (Supplementary Figure S2A, B), consistent with IF staining for Pol II, H3K9ac, and H3K9me3 and with qPCR results, which detected no overt abnormalities between *Hsf5*$^{-/-}$ and *Hsf5*$^{+/+}$ (Luo et al., 2024). Further analysis indicated that 35.3% (913/2 585) of up-regulated autosomal genes and 23.8% (10/42) of up-regulated XY-linked genes were associated with one or more open chromatin regions (Figure 1H), suggesting that the altered chromatin accessibility patterns in *Hsf5*$^{-/-}$ pachytene spermatocytes were weakly coupled to transcriptional activation. Specifically, although chromatins were more open in the absence of HSF5, the transcription of these genes did not increase accordingly. Notably, our findings, which show no strong correlation between chromatin accessibility and gene transcription in *Hsf5*$^{-/-}$, align with previous studies. For instance, (Maezawa et al., 2018) observed that, despite transcriptional silencing associated with MSCI, a substantial number of unique ATAC peaks appeared on the sex chromosomes. Similarly, (Miyamoto et al., 2018) emphasized that chromatin accessibility does not always correlate with transcriptional activity in oocytes. Furthermore, during the mid-pachytene stage, XY chromosomes do not exhibit DAPI-dense heterochromatin characteristics in cytological analyses (Supplementary Figure S2C), suggesting that transcriptional silencing of the XY chromosomes may not be linked to chromatin compaction, a finding also reported by (Alavattam et al., 2022).

TRN is altered in *Hsf5*$^{-/-}$ pachytene spermatocytes

Transcriptional reprogramming governed by the TRN plays a crucial role in ensuring the proper progression of pachynema and predicts both target gene expression and downstream biological processes (Carrell, 2008). Based on scRNA-seq data (eP, mP, and lP) and the TRRUST v2 database (Han et al., 2018; Luo et al., 2015), 190 transcription factors (TFs) involved in pachynema progression were identified, including *Hnrnpk*, *Ezh1*, *Hsf1*, and *Yy1* (Figure 2A). Because *Hsf5*$^{-/-}$ testes did not progress to lP (Luo et al., 2024), analyses focused on target downstream genes (TDGs) regulated by eP- and mP-enriched TFs that normally drive advancement to lP. Across these TFs, 1 092 TDGs were identified and classified as activated, repressed, or unknown based on regulation by upstream TFs (Figure 2B). Compared with *Hsf5*$^{+/+}$, *Hsf5*$^{-/-}$ pachytene cells exhibited two distinct TDG sets with marked changes: 108 down-regulated and 179 up-regulated genes, including meiotic regulators such as *Cdk1*, *Tcfl5*, and *Uhrf1* (Clement et al., 2015; Dong et al., 2019; Galán-Martínez et al., 2022). Based on Gene Ontology (GO) enrichment analysis, the 108 down-regulated TDGs were enriched in “negative regulation of apoptotic process”, “cell division”, and “chromatin remodeling”, while the 179 up-regulated TDGs were enriched in “chromatin remodeling”, “apoptotic process”, and “protein phosphorylation”. TRRUST v2 analysis showed that expression shifts tracked the annotated regulatory direction of upstream transcription factors. In the down-regulated TDG set, 39.8% (43/108) were annotated as repressed by their regulators, exceeding the 16.7% (18/108) annotated as activated. In the up-regulated set, 37.9% (68/179) were annotated as activated, nearly threefold the 12.8% (23/179) annotated as repressed. These distributions indicate that core transcription factor programs and the associated TRN coordinate pachynema progression, and that loss of HSF5 triggers network-wide dysregulation culminating in pachytene arrest.

Because accessible chromatin frequently harbors TF-binding sites (Buenrostro et al., 2013), the identified TFs were integrated with ATAC-seq profiles. Motif analysis with HOMER on regions that gained accessibility in *Hsf5*$^{-/-}$ identified a group of consensus motifs matching known sites in pachytene spermatocytes. The inferred regulators included factors essential for spermatogenesis, including nuclear factor Y (NFYA and NFYB) and members of the SOX and POU families (Hou et al., 2012; Wu et al., 2010). HOMER motif analysis identified TF families also highlighted in Figure 2A (SP, SOX, KIF, TCF; Figure 2C), and the targets of these factors overlapped meiosis-related TDGs in Figure 2B (e.g., *Ccnb1*, *Bsg*, *Setdb1*; Figure 2D), collectively indicating a remodeled transcriptional regulatory network in *Hsf5*$^{-/-}$ pachytene spermatocytes.

XY body formation and histone composition are altered in *Hsf5*$^{-/-}$ pachytene spermatocytes

To assess whether altered chromatin accessibility and TRN disruption were associated with changes in nucleosome composition and XY body formation in *Hsf5*$^{-/-}$ pachytene spermatocytes, nucleosomes were purified from *Hsf5*$^{+/+}$ and *Hsf5*$^{-/-}$ pachytene cells and the abundance of canonical histones and variants was quantified by Coomassie Brilliant Blue staining. Core histones H3 and H4 were comparable between genotypes (Figure 3A, black arrows), whereas H2 was reduced in *Hsf5*$^{-/-}$ nucleosomes (Figure 3A, red arrows, lower red asterisk). Histone H1 isoforms, reported to range from 25 to 35 kDa (Lin et al., 2024; Shechter et al., 2007), also displayed three bands in *Hsf5*$^{+/+}$ pachytene cells, whereas only two higher-molecular-mass bands were observed in *Hsf5*$^{-/-}$ pachytene cells (Figure 3A, blue arrows, upper red asterisk). Immunoblotting of whole-cell extracts corroborated these trends, revealing decreased H1t, γH2AX (Ser139-phosphorylated H2AX), and macroH2A.1 in *Hsf5*$^{-/-}$ pachytene

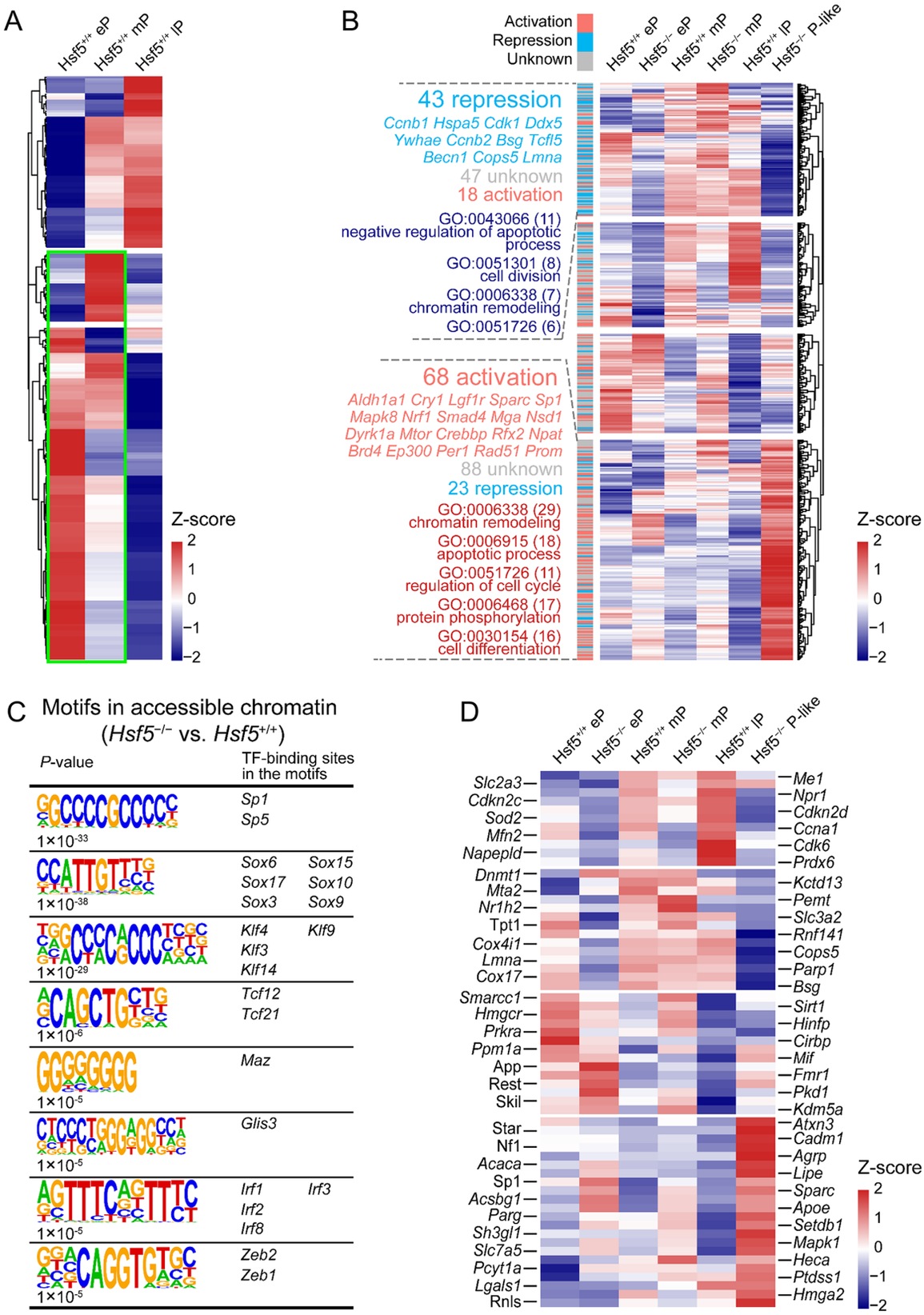

Figure 2 TRN alterations in *Hsf5*$^{-/-}$ pachytene spermatocytes

A: Heatmap showing TF expression patterns in spermatocytes during *Hsf5*$^{+/+}$ pachynema progression. Each row represents a gene; each column represents a single cell. B: Heatmap showing TDGs regulated by TFs (highlighted in green box in A) in *Hsf5*$^{+/+}$ and *Hsf5*$^{-/-}$ pachytene cells during pachynema. Each row represents a gene; each column represents a single cell. Leftmost column indicates regulatory annotation for each TDG (activated, repressed, unknown). C: HOMER motif enrichment of regions with increased ATAC-seq accessibility in *Hsf5*$^{-/-}$ pachytene cells, identifying putative TF-binding sites that overlap with factors in A. D: Heatmap showing expression patterns of TDGs regulated by TFs in C in *Hsf5*$^{+/+}$ and *Hsf5*$^{-/-}$ pachytene cells during pachytene. Each row represents a gene; each column represents a single cell.

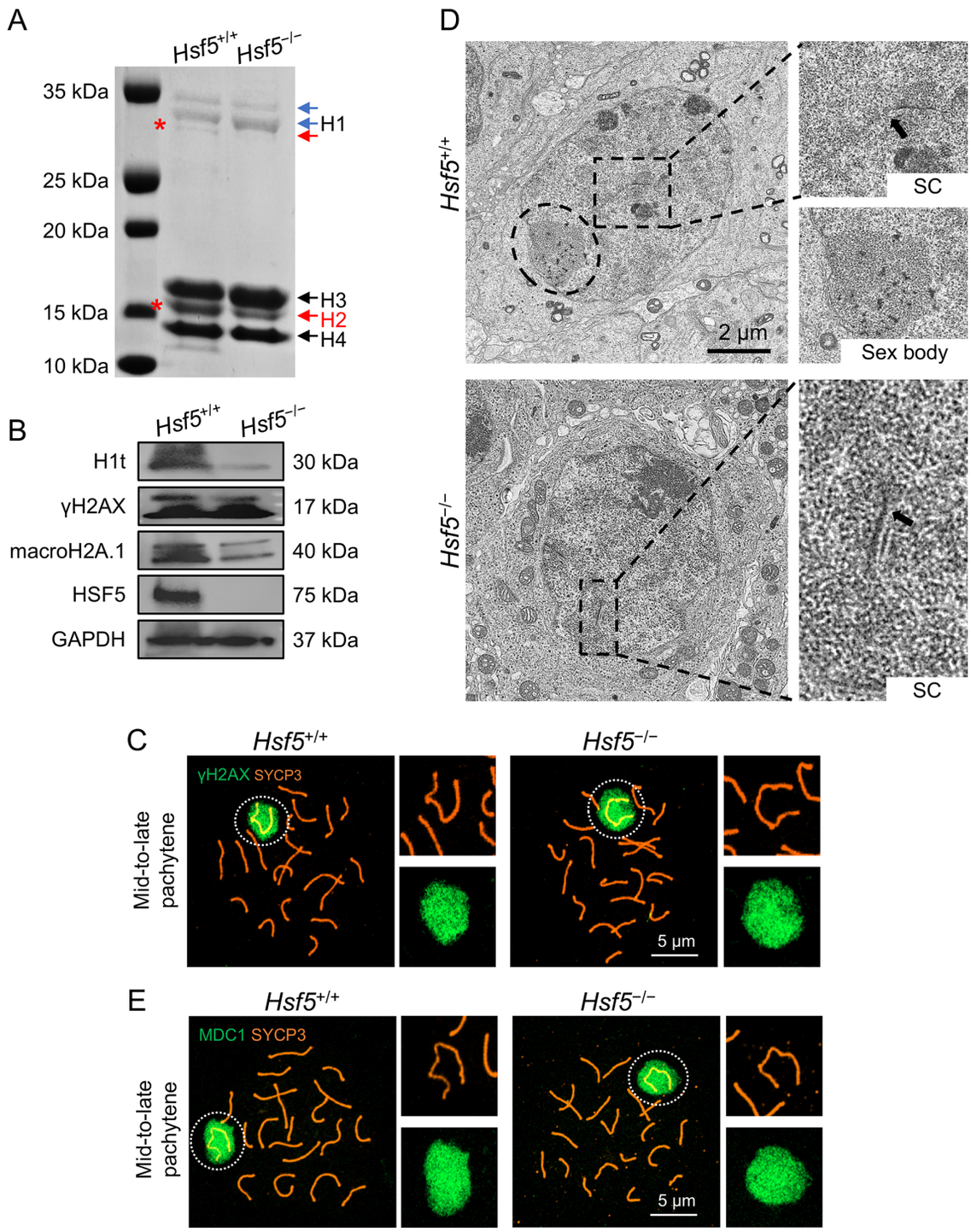

Figure 3 Nucleosome composition, TEM analysis, and γH2AX-MDC1 signaling pathway in *Hsf5*$^{+/+}$ and *Hsf5*$^{-/-}$ pachytene spermatocytes

A: Coomassie Brilliant Blue staining of purified nucleosomes from *Hsf5*$^{+/+}$ and *Hsf5*$^{-/-}$ pachytene cells. Red asterisks indicate altered histones. B: WB analysis of histone variants (H1t, γH2AX, and macroH2A.1) in *Hsf5*$^{+/+}$ and *Hsf5*$^{-/-}$ pachytene cells. GAPDH, loading control. C: SYCP3 was co-stained with γH2AX on chromosome spreads from P56 *Hsf5*$^{+/+}$ and *Hsf5*$^{-/-}$ mice. Dashed circles indicate sex chromosome area. Scale bar is shown. D: TEM images of representative pachytene spermatocytes in *Hsf5*$^{+/+}$ and *Hsf5*$^{-/-}$ mice. XY body (black dashed oval) and synaptonemal complex (SC, black dashed box) were observed in *Hsf5*$^{+/+}$ pachytene spermatocytes. XY body appeared as a round, lighter, and more homogeneous mass compared with other areas in the cell nucleus. In contrast, no distinct XY body was observed in *Hsf5*$^{-/-}$ pachytene spermatocytes, although SC (arrowhead) was still visible. Scale bar is shown. E: SYCP3 was co-stained with MDC1 on chromosome spreads from P56 *Hsf5*$^{+/+}$ and *Hsf5*$^{-/-}$ mice. Dashed circles indicate sex chromosome area. Scale bar is shown.

spermatocytes (Figure 3B). In contrast, nuclear spread IF detected similar H1t, γH2AX, and macroH2A.1 signals in both genotypes (Figure 3C; Supplementary Figure S3A, B). These observations indicate a role for HSF5 in establishing normal core and linker histone composition in pachytene spermatocytes. However, due to pachynema progression arrest, these changes could also be attributed to a biased distribution of meiotic substages in *Hsf5*$^{-/-}$ pachytene cells

(Supplementary Figure S3C).

Next, TEM was used to analyze nuclear ultrastructure and chromosome behavior. Synaptonemal complexes, formed between homologous autosomes and characterized by extruding condensed chromatin fibers, were evident in both *Hsf5*$^{+/+}$ and *Hsf5*$^{-/-}$ pachytene spermatocytes. In *Hsf5*$^{+/+}$ testes, the XY chromatin formed a characteristic XY body—an elliptical, lightly stained, homogeneous domain—observed in 58.7% (128/218) of cells (Figure 3D, black arrow). In adult *Hsf5*$^{-/-}$ testes, XY bodies were rare, present in only 5.9% (16/270) of sections showing XY body-like structures. Recruitment of DNA damage response (DDR) proteins to the sex chromosomes precedes XY body formation (Alavattam et al., 2022). Consistent with this sequence, γH2AX, MDC1, ATR, and BRCA1, core components of the DDR pathway, exhibited normal localization in both genotypes (Figure 3C, E; Supplementary Figure S3D, E). Together, these findings place HSF5 downstream of the γH2AX-MDC1 signaling pathway on meiotic sex chromosomes and indicate that HSF5 is required for proper compartmentalization of X and Y chromosomes into the XY body domain.

Defective epigenetic programming of meiotic sex chromosomes in the absence of HSF5

Meiotic sex chromosomes undergo extensive epigenetic reprogramming downstream of the γH2AX-MDC1 signaling pathway. Furthermore, because ubiquitin and SUMO modifications exhibit dynamic patterns during prophase I and regulate multiple meiotic processes in mice (Alavattam et al., 2022; Rao et al., 2017), SUMOylation and ubiquitylation were examined on sex chromosomes in *Hsf5*$^{-/-}$ pachytene spermatocytes. Signals detected with anti-SUMO1 and anti-SUMO2/3 antibodies accumulated at centromeric heterochromatin and across XY chromatin in pachynema, with no detectable differences between genotypes (Figure 4A, B). As ubiquitin modification regulatory impact depends on chain type (monoubiquitin or polyubiquitin) (Hasegawa et al., 2015), antibody clone E65C was used to detect RNF8-mediated H2A polyubiquitination, and clone FK2 was used to detect monoubiquitin and K29-, K48-, and K63-linked polyubiquitin chains (Hasegawa et al., 2015). At mid-to-late pachytene, FK2 and E65C signals were robust and encompassed the XY body in *Hsf5*$^{+/+}$ spermatocytes, with comparable patterns in *Hsf5*$^{-/-}$ spermatocytes (Figure 4C, D).

H2A monoubiquitination (H2AK119ub) and K48-linked ubiquitination (K48ub), two ubiquitin marks associated with meiotic regulation (Hasegawa et al., 2015; Luo et al., 2015; Rao et al., 2017), were profiled. In *Hsf5*$^{+/+}$ pachytene spermatocytes, H2AK119ub was not enriched within the XY body (Figure 4E), consistent with prior observations (Hasegawa et al., 2015). However, in *Hsf5*$^{-/-}$ pachytene spermatocytes, H2AK119ub was significantly up-regulated on the XY pair, with similar signals observed on autosomes compared with *Hsf5*$^{+/+}$ cells (Figure 4E). K48ub, which targets proteins for degradation via the ubiquitin-proteasome system (Rao et al., 2017), displayed diffuse nuclear distribution in *Hsf5*$^{+/+}$ pachytene cells (Figure 4F). Notably, K48ub signals were relatively reduced on the XY pair, with no obvious autosomal abnormalities (Figure 4F). These results suggest that HSF5 is differentially involved in the ubiquitin modification of XY chromosomes and autosomes, and that HSF5 deficiency may disrupt H2AK119ub and K48ub regulation on meiotic sex chromosomes.

To determine whether HSF5 deficiency and abnormal ubiquitination (H2AK119ub and K48ub) affected the distribution of other epigenetic modifications downstream of the γH2AX-MDC1 signaling pathway on meiotic sex chromosomes, additional histone marks were examined. In *Hsf5*$^{-/-}$ pachytene spermatocytes, the mono- and dimethylation of H3K9 (H3K9me1 and H3K9me2), as well as histone H3 acetylation at lysine 27 (H3K27ac), remained unchanged compared with *Hsf5*$^{+/+}$ cells (Supplementary Figure S4A–C). These data suggest that HSF5 participates in the regulation of ubiquitination of XY chromosomes, and disordered ubiquitination on XY chromosomes likely leads to the pachytene arrest and apoptotic cell death observed in *Hsf5*$^{-/-}$ spermatocytes (Luo et al., 2024).

***Hsf5*-deficient spermatocytes exhibit abnormal spermatoproteasome signals on meiotic sex chromosomes**

Reduced K48ub-linked ubiquitin on XY chromosomes, together with the role of K48ub chains in targeting proteins for degradation via the ubiquitin-proteasome system (Rao et al., 2017), termed the spermatoproteasome during spermatogenesis (Gómez et al., 2019), prompted examination of spermatoproteasome localization and activity in *Hsf5*$^{-/-}$ spermatocytes. Immunostaining for PSMB2 (β-type) and PSMA7 (α-type) subunits of the cylindrical catalytic core particle in proteasome complexes (Collins and Goldberg, 2017) revealed axis-associated signals that colocalized with SYCP3 on both sex chromosomes and autosomes in *Hsf5*$^{+/+}$ pachytene spermatocytes (Figure 4G, H). However, in *Hsf5*$^{-/-}$ spermatocytes, these signals were absent from the XY chromosomes, while similar signals were observed on autosomes compared with *Hsf5*$^{+/+}$ cells (Figure 4G, H). Proteasomal catalytic output in whole-cell extracts from pachytene spermatocytes was quantified by measuring chymotrypsin-like activity (associated with the β5 catalytic subunit), caspase-like activity (β1), and trypsin-like activity (β2) (Gomes et al., 2009). Biochemical analysis revealed comparable proteasomal activity in *Hsf5*$^{-/-}$ and *Hsf5*$^{+/+}$ extracts (Figure 4I). However, this equivalence does not exclude XY-specific alterations, as the presence of autosome-associated proteasomes could mask potential differences.

HSF5 functions as an E3 ligase or as a ubiquitination substrate

To test whether HSF5 functions as an E3 ligase or serves as a substrate for ubiquitination, HEK293T cells were co-transfected with pCMV6-HSF5-Flag and various expression plasmids: pCMV-HA-ubiquitin (wild-type, WT), pCMV-HA-ubiquitin (K48), in which all lysine residues, except for lysine at position 48, were mutated to arginine, and pCMV-HA-ubiquitin (K48R), where the lysine at position 48 was substituted with arginine. Cells were harvested 36 h after transfection for protein extraction. Whole-cell extracts (WCE) were immunoprecipitated using an anti-FLAG antibody to enrich HSF5 and its potential interacting partners. The WCE and immunoprecipitation eluates were then analyzed by WB for HA-ubiquitin detection. Co-expression of pCMV6-HSF5-Flag with HA-ubiquitin variants (WT, K48-only, K48R) generated HA-reactive ubiquitin conjugates across a broad molecular-weight range, whereas extracts lacking HA-ubiquitin or expressing HSF5 alone showed little or no signal (Figure 4J). Anti-FLAG immunoprecipitation enriched HA-ubiquitin in association with ectopic HSF5, while the pCMV6-HSF5-Flag-

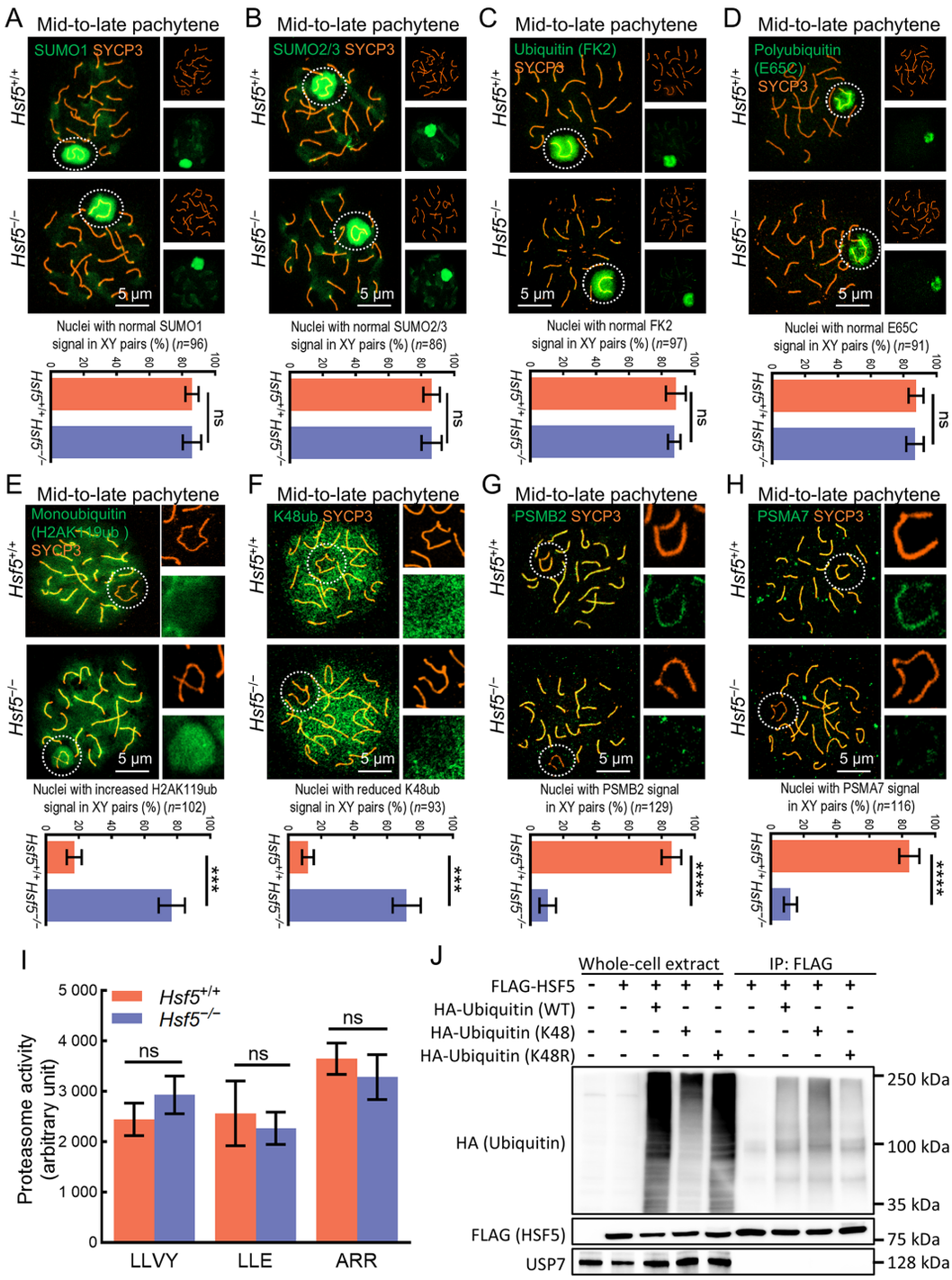

Figure 4 Epigenetic programming and spermatoproteasome signal analysis of meiotic sex chromosomes in *Hsf5*$^{-/-}$ pachytene spermatocytes

A–H: SYCP3 was co-stained with SUMO1, SUMO2/3, FK2, E65C, H2AK119ub, K48ub, PSMB2, and PSMA7 on chromosome spreads from P56 *Hsf5*$^{+/+}$ and *Hsf5*$^{-/-}$ mice. Dashed circles indicate sex chromosome area. Scale bars are shown. Three males were used in each experiment; *n*, number of pachytene spermatocytes analyzed. Data are presented as mean±SD; ns: Not significant; ***: $P<0.001$; ****: $P<0.0001$ (Mann-Whitney U test). I: Proteasome activity of *Hsf5*$^{+/+}$ and *Hsf5*$^{-/-}$ pachytene spermatocytes. Fluorescently labeled substrates LLVY, LLE, and ARR were used to detect chymotrypsin-like (β5 catalytic subunit), caspase-like (β1 catalytic subunit), and trypsin-like (β2 catalytic subunit) activities, respectively. Data were normalized to the background signal, with values obtained without protein subtracted for correction; ns: Not significant (two-way ANOVA). J: *In vivo* ubiquitylation assay showing substantial HA-tagged ubiquitin in association with ectopic HSF5 protein.

only control yielded minimal HA signal (Figure 4J). These findings indicate that HSF5 either catalyzes ubiquitin transfer or serves as a ubiquitination substrate, and that chain types are not restricted to K48 linkages.

HSF5-USP7 complex suppresses H2AK119ub on meiotic sex chromosomes *in vivo*

To investigate the basis for elevated H2AK119ub on meiotic sex chromosomes, enzymes mediating ubiquitination and

deubiquitination at H2A Lys119 were evaluated. RNF2, an E3 ubiquitin ligase within the polycomb repressive complex 1, is reported to mediate the addition of ubiquitin to H2AK119 (Wang et al., 2004). Conversely, the deubiquitinating enzyme USP7 removes ubiquitin from H2AK119 *in vitro*, thereby counteracting ubiquitination and potentially modulating chromatin dynamics (Maertens et al., 2010). RNF2 signals were axis-associated and colocalized with SYCP3, with no genotype-dependent differences between *Hsf5*$^{+/+}$ and *Hsf5*$^{-/-}$ pachytene spermatocytes (Figure 5A). In contrast, USP7 signals were strongly enriched on XY chromosomes in *Hsf5*$^{+/+}$ cells but were nearly absent from sex chromosomes in *Hsf5*$^{-/-}$ spermatocytes (Figure 5B). In P56 testis sections, USP7 colocalized with HSF5 and was highly enriched within the XY body in *Hsf5*$^{+/+}$ tubules (Figure 5C, white arrow), but was rarely detected in *Hsf5*$^{-/-}$ tubules, with only a few weak signals observed (Figure 5C, red arrow). Co-immunoprecipitation using whole-cell extracts from pachytene spermatocytes with

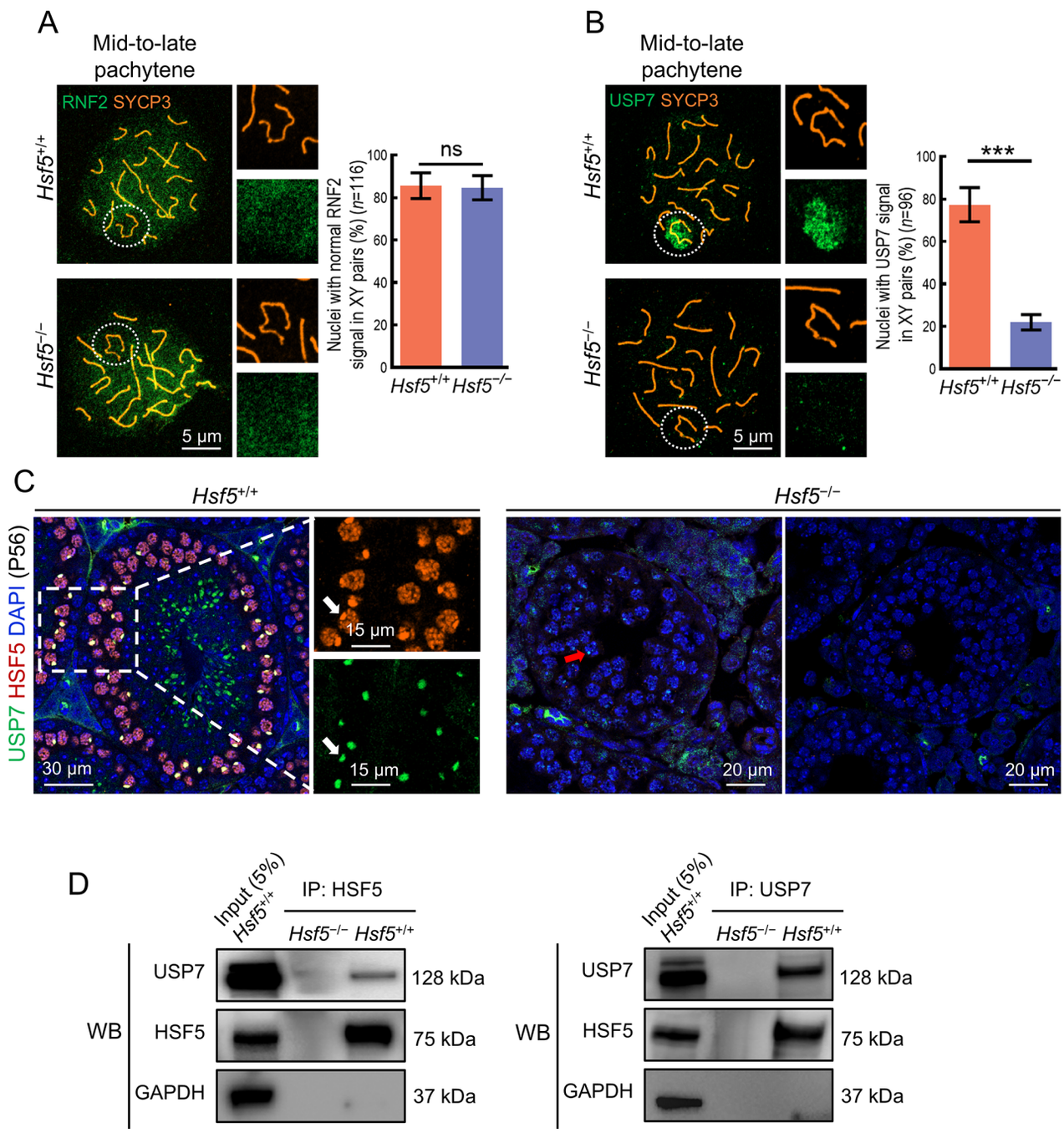

Figure 5 HSF5-USP7 complex suppresses H2AK119ub on meiotic sex chromosomes *in vivo*

A, B: SYCP3 was co-stained with RNF2 and USP7 on chromosome spreads from P56 *Hsf5*$^{+/+}$ and *Hsf5*$^{-/-}$ mice. Dashed circles indicate sex chromosome area. Scale bars are shown. Three males were used in each experiment; *n*, number of pachytene spermatocytes analyzed. Data are presented as mean±SD; ns: Not significant; ***: $P<0.001$ (Mann-Whitney *U* test). C: USP7 was co-stained with HSF5 on testis sections from P56 *Hsf5*$^{+/+}$ and *Hsf5*$^{-/-}$ mice. Gray arrow indicates XY body, where HSF5 and USP7 were highly enriched and colocalized in *Hsf5*$^{+/+}$ cells. In contrast, USP7 signals were absent or weak in *Hsf5*$^{-/-}$ cells, as indicated by red arrow. Scale bars are shown. D: Co-IP of HSF5 with USP7 in *Hsf5*$^{+/+}$ pachytene spermatocytes. GAPDH, loading control.

rabbit anti-HSF5 and anti-USP7 antibodies confirmed an association between HSF5 and USP7 in *Hsf5*$^{+/+}$ but not *Hsf5*$^{-/-}$ samples (Figure 5D). This interaction was not detectable after HSF5 overexpression from pCMV6-HSF5-Flag in cultured cells (Figure 4J). These data support formation of an endogenous HSF5-USP7 complex on meiotic sex chromosomes in vivo that likely constrains H2AK119ub on the XY pair.

In summary, integrated multi-omics and cell biology analyses revealed an indispensable role of HSF5 for proper chromatin behavior and transcriptional reprogramming to drive pachynema progression (Figure 6). Loss of *Hsf5* leads to a more open chromatin state, triggering a cascade of abnormal TRN responses, defective XY body formation, altered histone composition, decreased XY-linked K48ub and spermatoproteasome signals, and increased H2AK119ub on XY chromatin, ultimately resulting in pachytene arrest. The evidence supports a dual role for HSF5 during pachynema progression, acting either as an E3 ligase or ubiquitination substrate on XY chromatin, or interacting with USP7 to suppress XY-linked H2AK119ub.

DISCUSSION

Meiosis is critical for the production of gametes, ensuring genetic diversity and the proper segregation of chromosomes. In this study, testis-specific protein HSF5 was identified as essential for the coordination of chromatin dynamics and transcriptional reprogramming during pachynema progression. Integrated multi-omics and cell biology analyses delineated how HSF5 shapes accessibility landscapes, histone composition, XY body architecture, and ubiquitin-based signaling on sex chromosomes.

ATAC-seq revealed widespread remodeling of chromatin accessibility after *Hsf5* deletion, with a global increase in open chromatin regions, particularly at TSSs. These shifts may impact the binding of TFs and other regulatory proteins, ultimately disrupting the TRN. Concordant changes in histone composition and abnormal XY body formation in *Hsf5*$^{-/-}$ pachytene spermatocytes further implicate HSF5 in chromatin remodeling during pachynema, as reported in previous studies. Notably, while proper XY body formation was not observed in *Hsf5*$^{-/-}$ pachytene spermatocytes, normal γH2AX and MDC1 signals were detected on the sex chromosomes, suggesting that DDR-directed meiotic silencing in early MSCI precedes HSF5-mediated XY body formation (although DDR-directed silencing does not always coincide with XY body formation). Loss of HSF5 also led to abnormal ubiquitination patterns on meiotic sex chromosomes, characterized by increased H2AK119ub and decreased K48ub signals on the XY chromosomes, suggesting that HSF5 differentially regulates ubiquitin modification on XY chromosomes and autosomes. Mechanistically, the data support a model in which HSF5 either participates directly in ubiquitination on XY chromatin (as an E3 ligase or as a substrate) and/or cooperates with USP7 to restrain H2AK119ub, thereby maintaining an epigenetic environment permissive for pachynema progression.

Several questions remain to be answered. First, current TF

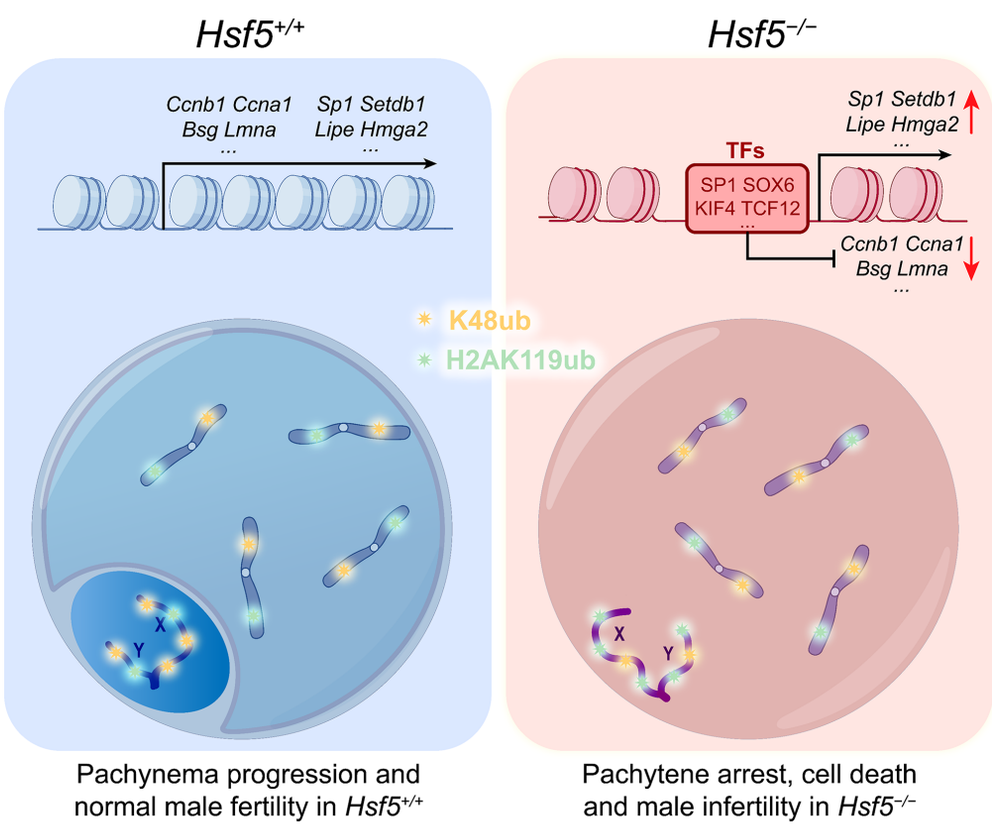

Figure 6 Pachytene development in fertile mice vs. pachytene arrest in *Hsf5*$^{-/-}$ infertile mice

Deletion of *Hsf5* leads to altered histone composition and a more open chromatin state, with TFs such as the SP, SOX, KIF, and TCF families being abnormally enriched, triggering a cascade of aberrant TRN responses, including down-regulation of genes such as *Ccnb1*, *Ccna1*, *Bsg*, and *Lmna*, and up-regulation of genes such as *Sp1*, *Setdb1*, *Lipe*, and *Hmga2*. Additionally, deletion of *Hsf5* leads to defective XY body formation, decreased XY-linked K48ub, and increased H2AK119ub on XY chromatin, ultimately resulting in pachytene arrest.

repositories and TF–target maps are incomplete. Notably, many genes cannot yet be assigned to upstream TFs, and regulation of numerous TDGs remains unresolved. For example, HSPA2, SYCP1, and MEIOB, previously implicated in pachynema (Luo et al., 2024), were not identified through integrated analysis of the TRRUST v2 database and HOMER. Motif-based inference requires expanded annotations and targeted validation to define TRN architecture during pachynema. Second, the causal links among increased chromatin accessibility, altered epigenetic modification, failure of XY body formation, and TRN disruption in *Hsf5*$^{-/-}$ pachytene spermatocytes remain to be established. XY body assembly requires coordinated chromatin compaction, histone modifications, LLPS, and higher-order genome organization, which induce X and Y chromosome proximity during meiosis (Handel, 2020; Hildebrand and Dekker, 2020). Recent studies have indicated that transcription is regulated not only by proteins binding to specific DNA sequences but also by 3D genome-based regulatory networks that integrate long-range chromatin contacts, epigenetic states, and condensate dynamics (Stadhouders et al., 2019; Su et al., 2020; Tian et al., 2022) (Stam et al., 2019; Zheng and Xie, 2019). Comprehensive mapping of 3D genome architecture in *Hsf5*$^{-/-}$ pachytene spermatocytes should provide valuable insights into the complex and intricate molecular processes driving pachynema progression. Third, the molecular mechanisms underlying meiosis are extraordinarily complex and remain incompletely understood. While C57BL/6J mice remain the most feasible model given current technological and experimental conditions, extrapolation across mammals and consideration of genomic conflicts will require additional models to better illustrate the role of HSF5 in pachynema progression.

DATA AVAILABILITY

The ATAC-seq data reported in this study have been deposited in the Genome Sequence Archive (GSA) at the National Genomics Data Center and China National Center for Bioinformation (https://ngdc.cncb.ac.cn/gsa; accession number GSA: CRA023389), Science Data Bank (https://doi.org/10.57760/sciencedb.21518), and NCBI Sequence Read Archive (SRA; https://www.ncbi.nlm.nih.gov/sra; BioProjectID PRJNA1205528). All other data supporting the conclusions of this study are available from the corresponding author upon reasonable request.

SUPPLEMENTARY DATA

Supplementary data to this article can be found online.

COMPETING INTERESTS

The authors declare that they have no competing interests.

AUTHORS' CONTRIBUTIONS

F.S., J.F.Z., C.H.L., and C.X. conceptualized the study; C.H.L. designed and performed experiments and analyzed data. Z.Q.Y., C.H.L., and Z.W.F. performed bioinformatic analyses; C.H.L., D.L.L., H.R.X., S.M.Z., X.J.Z., H.C.L., L.F.S., and Z.A.L. participated in methodology development and investigation. C.H.L., Z.Q.Y., and Z.W.F. performed visualizations; C.H.L. wrote the original manuscript; all authors contributed to this work, discussed the results, critically reviewed and revised the manuscript. All authors read and approved the final version of the manuscript.

ACKNOWLEDGEMENTS

We are grateful to the members of the Sun Laboratory for helpful discussions and comments. We also thank Figdraw (www.figdraw.com) for assistance in creating Figure 6.

REFERENCES

Abe H, Alavattam KG, Hu YC, et al. 2020. The initiation of meiotic sex chromosome inactivation sequesters DNA damage signaling from autosomes in mouse spermatogenesis. *Current Biology*, **30**(3): 408–420. e5.

Alavattam KG, Maezawa S, Andreassen PR, et al. 2022. Meiotic sex chromosome inactivation and the XY body: a phase separation hypothesis. *Cellular and Molecular Life Sciences*, **79**(1): 18.

Amemiya HM, Kundaje A, Boyle AP. 2019. The ENCODE blacklist: identification of problematic regions of the genome. *Scientific Reports*, **9**(1): 9354.

Blanco-Rodríguez J. 2009. γH2AX marks the main events of the spermatogenic process. *Microscopy Research and Technique*, **72**(11): 823–832.

Buenrostro JD, Giresi PG, Zaba LC, et al. 2013. Transposition of native chromatin for fast and sensitive epigenomic profiling of open chromatin, DNA-binding proteins and nucleosome position. *Nature Methods*, **10**(12): 1213–1218.

Carrell DT. 2008. Elucidating the genetics of male infertility: understanding transcriptional and translational regulatory networks involved in spermatogenesis. *International Journal of Andrology*, **31**(5): 455–456.

Chen SF. 2023. Ultrafast one-pass FASTQ data preprocessing, quality control, and deduplication using fastp. *iMeta*, **2**(2): e107.

Clement TM, Inselman AL, Goulding EH, et al. 2015. Disrupting cyclin dependent kinase 1 in spermatocytes causes late meiotic arrest and infertility in mice. *Biology of Reproduction*, **93**(6): 137.

Collins GA, Goldberg AL. 2017. The logic of the 26S proteasome. *Cell*, **169**(5): 792–806.

Corces MR, Trevino AE, Hamilton EG, et al. 2017. An improved ATAC-seq protocol reduces background and enables interrogation of frozen tissues. *Nature Methods*, **14**(10): 959–962.

Da Cruz I, Rodríguez-Casuriaga R, Santiñaque FF, et al. 2016. Transcriptome analysis of highly purified mouse spermatogenic cell populations: gene expression signatures switch from meiotic-to postmeiotic-related processes at pachytene stage. *BMC Genomics*, **17**: 294.

Dia F, Strange T, Liang J, et al. 2017. Preparation of meiotic chromosome spreads from mouse spermatocytes. *Journal of Visualized Experiments*, (129): 55378.

Dobin A, Davis CA, Schlesinger F, et al. 2013. STAR: ultrafast universal RNA-seq aligner. *Bioinformatics*, **29**(1): 15–21.

Dong J, Wang XL, Cao CC, et al. 2019. UHRF1 suppresses retrotransposons and cooperates with PRMT5 and PIWI proteins in male germ cells. *Nature Communications*, **10**(1): 4705.

Galán-Martínez J, Berenguer I, Del Carmen Maza M, et al. 2022. TCFL5 deficiency impairs the pachytene to diplotene transition during spermatogenesis in the mouse. *Scientific Reports*, **12**(1): 10956.

Goetz P, Chandley AC, Speed RM. 1984. Morphological and temporal sequence of meiotic prophase development at puberty in the male mouse. *Journal of Cell Science*, **65**: 249–263.

Gomes AV, Young GW, Wang YJ, et al. 2009. Contrasting proteome biology and functional heterogeneity of the 20 S proteasome complexes in mammalian tissues. *Molecular & Cellular Proteomics*, **8**(2): 302–315.

Gómez-H L, Felipe-Medina N, Condezo YB, et al. 2019. The PSMA8 subunit of the spermatoproteasome is essential for proper meiotic exit and mouse fertility. *PLoS Genetics*, **15**(8): e1008316.

Green CD, Ma QY, Manske GL, et al. 2018. A comprehensive roadmap of murine spermatogenesis defined by single-cell RNA-seq. *Developmental Cell*, **46**(5): 651–667. e10.

Guo M, Luo CH, Wang ZQ, et al. 2022. Uncoupling transcription and translation through miRNA-dependent poly(A) length control in haploid male germ cells. *Development*, **149**(12): dev199573.

Hamazaki N, Kyogoku H, Araki H, et al. 2021. Reconstitution of the oocyte transcriptional network with transcription factors. *Nature*, **589**(7841): 264–269.

Han H, Cho JW, Lee S, et al. 2018. TRRUST v2: an expanded reference database of human and mouse transcriptional regulatory interactions. *Nucleic Acids Research*, **46**(D1): D380–D386.

Handel MA. 2004. The XY body: a specialized meiotic chromatin domain. *Experimental Cell Research*, **296**(1): 57–63.

Handel MA. 2020. The XY body: an attractive chromatin domain. *Biology of Reproduction*, **102**(5): 985–987.

Hasegawa K, Sin HS, Maezawa S, et al. 2015. SCML2 establishes the male germline epigenome through regulation of histone H2A ubiquitination. *Developmental Cell*, **32**(5): 574–588.

Heinz S, Benner C, Spann N, et al. 2010. Simple combinations of lineage-determining transcription factors prime cis-regulatory elements required for macrophage and B cell identities. *Molecular Cell*, **38**(4): 576–589.

Hildebrand EM, Dekker J. 2020. Mechanisms and functions of chromosome compartmentalization. *Trends in Biochemical Sciences*, **45**(5): 385–396.

Hong SH, Shen XZ, Luo CH, et al. 2022. Comparative analysis of the testes from wild-type and *Alkbh5*-knockout mice using single-cell RNA sequencing. *G3 Genes*| *Genomes*| *Genetics*, **12**(8): jkac130.

Hou Y, Yuan J, Zhou X, et al. 2012. DNA demethylation and USF regulate the meiosis-specific expression of the mouse *Miwi*. *PLoS Genetics*, **8**(5): e1002716.

Ichijima Y, Ichijima M, Lou ZK, et al. 2011. MDC1 directs chromosome-wide silencing of the sex chromosomes in male germ cells. *Genes & Development*, **25**(9): 959–971.

Li H, Handsaker B, Wysoker A, et al. 2009. The sequence alignment/map format and SAMtools. *Bioinformatics*, **25**(16): 2078–2079.

Lin ZX, Li DL, Zheng JH, et al. 2024. The male pachynema-specific protein MAPS drives phase separation *in vitro* and regulates sex body formation and chromatin behaviors *in vivo*. *Cell Reports*, **43**(1): 113651.

Luo CH, Xu HR, Yu ZQ, et al. 2024. Meiotic chromatin-associated HSF5 is indispensable for pachynema progression and male fertility. *Nucleic Acids Research*, **52**(17): 10255–10275.

Luo MC, Zhou J, Leu NA, et al. 2015. Polycomb protein SCML2 associates with USP7 and counteracts histone H2A ubiquitination in the XY chromatin during male meiosis. *PLoS Genetics*, **11**(1): e1004954.

Maertens GN, El Messaoudi-Aubert S, Elderkin S, et al. 2010. Ubiquitin-specific proteases 7 and 11 modulate Polycomb regulation of the *INK4a* tumour suppressor. *The EMBO Journal*, **29**(15): 2553–2565.

Maezawa S, Yukawa M, Alavattam KG, et al. 2018. Dynamic reorganization of open chromatin underlies diverse transcriptomes during spermatogenesis. *Nucleic Acids Research*, **46**(2): 593–608.

Miyamoto K, Nguyen KT, Allen GE, et al. 2018. Chromatin accessibility impacts transcriptional reprogramming in oocytes. *Cell Reports*, **24**(2): 304–311.

Page J, De La Fuente R, Manterola M, et al. 2012. Inactivation or non-reactivation: what accounts better for the silence of sex chromosomes during mammalian male meiosis?. *Chromosoma*, **121**(3): 307–326.

Ramírez F, Ryan DP, Grüning B, et al. 2016. deepTools2: a next generation web server for deep-sequencing data analysis. *Nucleic Acids Research*, **44**(W1): W160–W165.

Rao HBDP, Qiao HY, Bhatt SK, et al. 2017. A SUMO-ubiquitin relay recruits proteasomes to chromosome axes to regulate meiotic recombination. *Science*, **355**(6323): 403–407.

Rathke C, Baarends WM, Awe S, et al. 2014. Chromatin dynamics during spermiogenesis. *Biochimica et Biophysica Acta (BBA) - Gene Regulatory Mechanisms*, **1839**(3): 155–168.

Roeder GS, Bailis JM. 2000. The pachytene checkpoint. *Trends in Genetics*, **16**(9): 395–403.

Ross-Innes CS, Stark R, Teschendorff AE, et al. 2012. Differential oestrogen receptor binding is associated with clinical outcome in breast cancer. *Nature*, **481**(7381): 389–393.

Shechter D, Dormann HL, Allis CD, et al. 2007. Extraction, purification and analysis of histones. *Nature Protocols*, **2**(6): 1445–1457.

Shima JE, Mclean DJ, Mccarrey JR, et al. 2004. The murine testicular transcriptome: characterizing gene expression in the testis during the progression of spermatogenesis. *Biology of Reproduction*, **71**(1): 319–330.

Stadhouders R, Filion GJ, Graf T. 2019. Transcription factors and 3D genome conformation in cell-fate decisions. *Nature*, **569**(7756): 345–354.

Stam M, Tark-Dame M, Fransz P. 2019. 3D genome organization: a role for phase separation and loop extrusion?. *Current Opinion in Plant Biology*, **48**: 36–46.

Su JH, Zheng P, Kinrot SS, et al. 2020. Genome-scale imaging of the 3D organization and transcriptional activity of chromatin. *Cell*, **182**(6): 1641–1659. e26.

Tahmasbpour Marzouni E, Ilkhani H, Beigi Harchegani A, et al. 2022. Epigenetic modifications, a new approach to male infertility etiology: a review. *International Journal of Fertility & Sterility*, **16**(1): 1–9.

Tian L, Liu T, Hua KJ, et al. 2022. The spatial organization of bacterial transcriptional regulatory networks. *Microorganisms*, **10**(12): 2366.

Turner JMA. 2015. Meiotic silencing in mammals. *Annual Review of Genetics*, **49**: 395–412.

Wang HB, Wang LJ, Erdjument-Bromage H, et al. 2004. Role of histone H2A ubiquitination in Polycomb silencing. *Nature*, **431**(7010): 873–878.

Wang HQ, Wu XL, Zhang J, et al. 2024. Meiotic transcriptional reprogramming mediated by cell-cell communications in humans and mice revealed by scATAC-seq and scRNA-seq. *Zoological Research*, **45**(3): 601–616.

Wang QW, Li M, Wu TZ, et al. 2022. Exploring epigenomic datasets by ChIPseeker. *Current Protocols*, **2**(10): e585.

Wu X, Oatley JM, Oatley MJ, et al. 2010. The POU domain transcription factor POU3F1 is an important intrinsic regulator of GDNF-induced survival and self-renewal of mouse spermatogonial stem cells. *Biology of Reproduction*, **82**(6): 1103–1111.

Wu XL, Luo CH, Hu LF, et al. 2020. Unraveling epigenomic abnormality in azoospermic human males by WGBS, RNA-Seq, and transcriptome profiling analyses. *Journal of Assisted Reproduction and Genetics*, **37**(4): 789–802.

Xie CB, Wang WL, Tu CF, et al. 2022. Meiotic recombination: insights into its mechanisms and its role in human reproduction with a special focus on non-obstructive azoospermia. *Human Reproduction Update*, **28**(6): 763–797.

Zhang BB, Ma H, Khan T, et al. 2020. A *DNAH17* missense variant causes flagella destabilization and asthenozoospermia. *Journal of Experimental Medicine*, **217**(2): e20182365.

Zheng H, Xie W. 2019. The role of 3D genome organization in development and cell differentiation. *Nature Reviews Molecular Cell Biology*, **20**(9): 535–550.

Zickler D, Kleckner N. 2015. Recombination, Pairing, and Synapsis of Homologs during Meiosis. *Cold Spring Harbor Perspectives in Biology*, **7**(6): a016626.